

3.3.2 LTSK1

Atmospheric Correction and Reflectance Algorithm

A. Algorithm Outline

- (1) Algorithm Code: LTSK 1
- (2) Product Code: ACLC
- (3) PI names: G18 Dr. Alfredo Huete
- (4) Overview of algorithm (Standard level)

Algorithm objectives

The algorithm has the following objective:

To atmospherically correct the composited, normalized radiances for "Rayleigh scattering and ozone absorption" on a per-pixel basis.

B. Theoretical Description

(1) Methodology and Logic Flow

A general flowchart describing atmosphere correction is presented in figure 1. Atmospheric correction is performed after the temporal mosaicking to reduce processing loads and disk space as only one image is processed every composite period (16-day). Rayleigh scattering and ozone absorption are corrected with the assistance of ancillary data provided by GAIT, such as the TOVS data set and GTOPO30. Much of the computation during atmospheric correction requires intensive CPU time due to floating point processing.

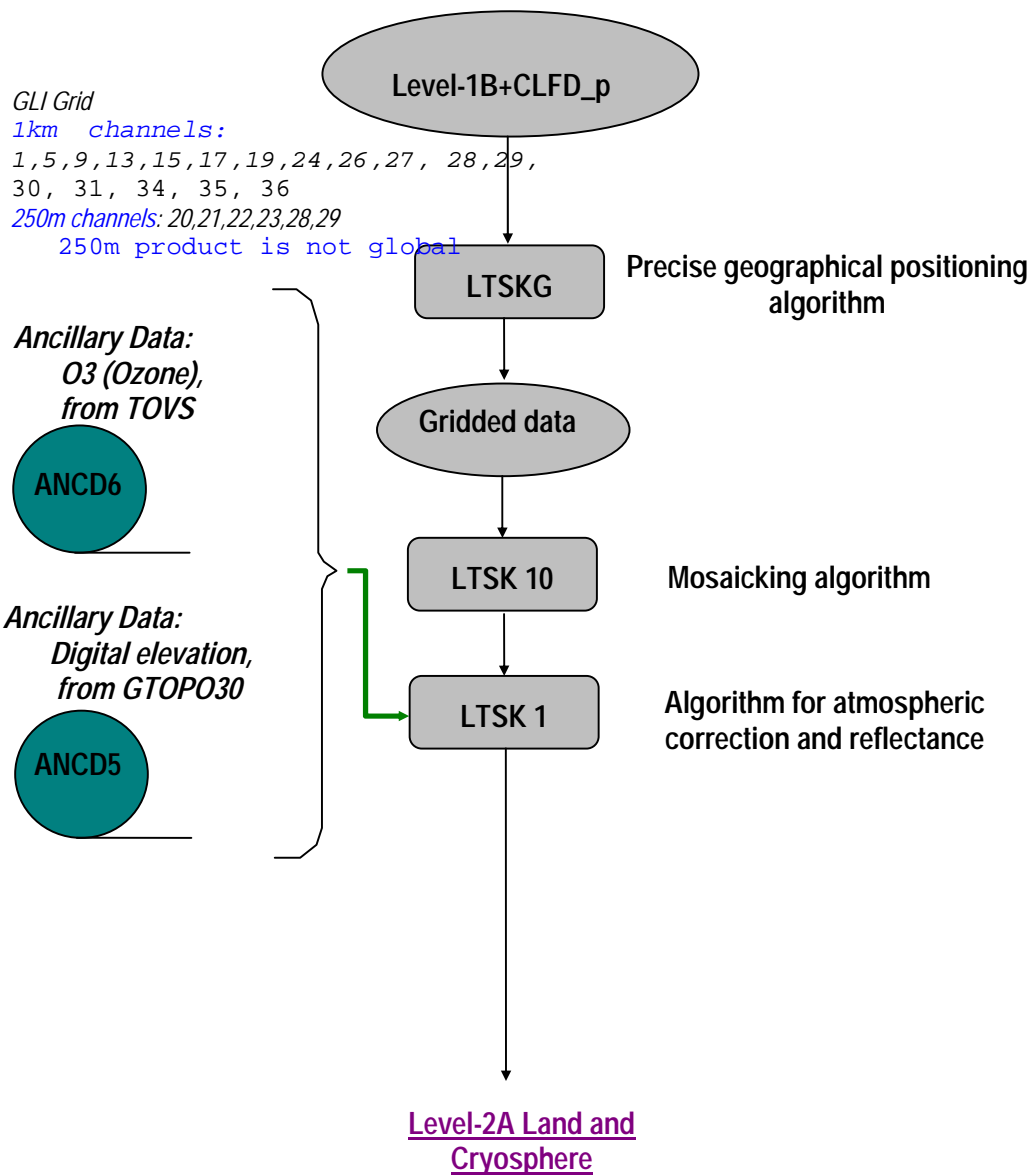


Figure 1: Flow diagram for the Atmospheric Correction and Reflectance Algorithm(LTSK1).

(2) Physical and Mathematical Aspects of the Algorithms

Atmospheric Radiative Transfer Modeling Algorithm

2.1 Introduction

We developed a set of computational procedures to fully solve for the radiation field at any arbitrary level within a planetary atmosphere. The polarization and intensity of the scattered light can be determined as functions of normal optical depth and viewing angle for varying mixtures of gaseous, aerosol and Rayleigh components.

There has been heightened awareness, especially in the last several years, of the crucial role that haze and clouds play in the complicated, coupled processes governing the Earth's atmospheric energy budget. Therefore, the need for detailed models that fully account for the transfer of visible and infrared radiation in the presence of small particles is particularly urgent. It is now becoming recognized that there is a definite involvement of both anthropogenically produced gaseous compounds and naturally occurring aerosols (via volcanic eruptions) in altering the chemical and radiative structure of the stratosphere and upper troposphere.

Although the scientific literature abounds with treatises which give many detailed formalisms for finding either the intensity or polarization (or sometimes both) of the sunlit sky in *ideal* circumstances, attempts to merge the mathematical complexities of polarized Rayleigh and Mie multiple scattering for real planetary atmospheres have been reported far less often. The current attempt to construct a reliable methodology for a complete calculation of both the intensity and polarization of light in an actual atmosphere should be a practical aid to those workers in climatology, i.e., who might like some guidelines in the area of computational radiative transfer.

2.2 Multiple Scattering with Polarization

- **Methodology**

The well-known radiative transfer equation (RTE) formulated by Chandrasekhar (1960) serves as the starting point for our investigations. In its integro-differential form it is written as:

$$\mu \frac{dI(\tau; \mu, \phi)}{d\tau} = I(\tau; \mu, \phi) - J(\tau; \mu, \phi)$$

In our treatment of the problem, the intensity I (photons $\text{cm}^{-2} \text{sec}^{-1} \text{sr}^{-1}$) is a 4-element vector, the Stokes vector, defined as:

$$I(\tau; \mu, \phi) = (I_l + I_r, I_l - I_r, U, V),$$

where I_{\parallel} and I_{\perp} are the components of the polarized intensities oriented parallel and perpendicular to the scattering plane. The parameter U is associated with the angle between the maximal electric field vibration direction and the plane of scattering, while V provides a measure of the degree of elliptical polarization of the wave. The usual phase function is replaced by a 4 x 4 phase matrix, $\tilde{\mathbf{P}}$. The intensity of the incident unattenuated solar beam (\mathbf{F}_0) is normalized to unity, and is equal to (1,0,0,0) for unpolarized light. The vertical optical depth is given by τ . At the top of the atmosphere $\tau = 0$. The quantity ω , a function of optical depth, is the single scattering albedo. The cosine of the observation zenith angle is designated as μ . The azimuth angle of the observations is ϕ .

The second quantity on the right-hand side of the RTE is the so-called source function, which in our vectorial representation is given by:

$$J(\tau; \mu, \phi) = \frac{1}{4\pi} \int_{-1}^1 \int_0^{2\pi} \tilde{\mathbf{P}}(\mu, \mu', \phi, \phi') I d\mu' d\phi' + \frac{\omega}{4} e^{\tau/\mu_0} \tilde{\mathbf{P}}(\mu, \mu_0, \phi, \phi_0) F_0$$

The second term on the right-hand side of this expression is recognized as the contribution to the source function arising from single scattering of the direct solar beam. It is to be noted that μ_0 is always intrinsically negative in these formulations.

- **Rayleigh Phase Matrix**

Written in terms of the scattering angle (θ), which is the angle between the scattered ray and the direction of the incident solar beam, the phase matrix for Rayleigh scattering is:

$$\tilde{\mathbf{P}}_{Ray}(\theta) = \begin{pmatrix} \frac{3}{4}(1 + \cos^2 \theta) & -\frac{3}{4}\sin^2 \theta & 0 & 0 \\ -\frac{3}{4}\sin^2 \theta & \frac{3}{4}(1 + \cos^2 \theta) & 0 & 0 \\ 0 & 0 & \frac{3}{2}\cos\theta & 0 \\ 0 & 0 & 0 & \frac{3}{2}\cos\theta \end{pmatrix}$$

- **Particle Phase Functions and Matrices**

In general, the phase matrix for an ensemble of spherical aerosol particles can be written in the form:

$$\tilde{P}_{Mie}(\theta) = \begin{pmatrix} P_{11} & P_{12} & 0 & 0 \\ P_{21} & P_{22} & 0 & 0 \\ 0 & 0 & P_{33} & P_{34} \\ 0 & 0 & P_{43} & P_{44} \end{pmatrix}$$

- **Necessary Transformations for Handling Polarization**

Two successive mathematical rotation operations on the scattering phase matrices need to be applied so that the resultant Stokes intensity components will be properly referenced to a coordinate system defined by the meridian plane. It is desirable to do this even in the case of single scattering, and absolutely imperative that it be done for the multiple scattering problem.

Liou (1980) presents a lucid explanation of the steps to follow. The resultant phase matrix referred to the meridian plane is:

$$\tilde{P}(\mu, \phi, \mu', \phi') = \tilde{L}(\pi - i_2) \tilde{P}(\theta) \tilde{L}(-i_1)$$

where the rotation angles are i_1 and i_2 . The matrix \tilde{L} gives the Stokes parameters in our new primed system. We have:

$$(I', Q', U', V') = \tilde{L}(\psi)(I, Q, U, V)$$

where

$$\tilde{L}(\psi) = \begin{pmatrix} 1 & 0 & 0 & 0 \\ 0 & \cos 2\psi & -\sin 2\psi & 0 \\ 0 & \sin 2\psi & \cos 2\psi & 0 \\ 0 & 0 & 0 & 1 \end{pmatrix}$$

The angle ψ can be found in Hansen and Travis (1974).

2.3 Description of the Gauss-Seidel Iteration Technique

For an arbitrary set of linear equations, Gauss-Seidel (G-S) iteration provides a powerful and relatively rapid means of obtaining an accurate solution to the algebraic system. Its main distinguishing feature is that the most recently calculated value of an unknown from the previous step is used to update the value of the variable in the new step. In any application of G-S, an initial estimate of the unknowns must be made. One notable example of the earliest use of G-S in

radiative transfer problems is the work of Herman and Browning (1965). The procedure we follow is patterned directly after their treatment. The atmosphere is divided into a number of layers each of optical depth $\Delta\tau$. Working with the integrated radiative transfer equation written in central differencing notation, we begin to march downward from the top of the atmosphere ($\tau=0$) to the bottom ($\tau = \tau_T$), solving for the individual Stokes parameters at every level (L) for a pre-selected set of observation directions specified by the pair (μ, ϕ) . The governing equation for the downward traverse is:

$$I^{L+1}(\tau; \mu, \phi) \approx I^{L-1}(\tau; \mu, \phi)e^{-2\Delta\tau/\mu} + (1 - e^{-2\Delta\tau/\mu})J^i(\tau; \mu, \phi)$$

with J^i being the average source term (a 4-element vector in our polarized rendition) within layer i . Recall that it is given as:

$$J^i(\tau; \mu, \phi) = \frac{1}{4\pi} \int_{-1}^1 \int_0^{2\pi} \tilde{P}(\mu, \mu', \phi, \phi') I^i d\mu' d\phi' + \frac{\omega}{4} e^{\tau/\mu_0} \tilde{P}(\mu, \mu_0, \phi, \phi_0) F_0$$

A 2-point boundary condition applies to this problem so that there is no downward diffuse intensity at the top of the atmosphere nor any upwardly directed contribution at the bottom. When the bottom of the atmosphere is reached, a completely analogous equation, with μ changed to $-\mu$, is written for the upward traverse, namely:

$$I^{L-1}(\tau; \mu, \phi) \approx I^{L+1}(\tau; \mu, \phi)e^{-2\Delta\tau/\mu} + (1 - e^{-2\Delta\tau/\mu})J^i(\tau; \mu, \phi)$$

The last computed downward intensity is used in the calculation of the first upward intensity. Though no actual convergence criteria were specified in the development and testing of the codes, it became apparent that virtually constant values of a sufficient set of diagnostic intensities were achieved quite quickly for small total optical depths. In most instances only a few iterations were required for a well-converged solution. For each cycle in the march through the atmosphere, an energy conservation test is applied, i.e., we must require that the total incident solar flux balance the scattered flux emerging from the top of the atmosphere plus the flux transmitted to the ground. For a wide range of simulations we were able to conserve more than 99 percent of the flux.

2.4 Verification of Rayleigh Multiple Scattering Calculations

What pattern should be expected for the variation in the intensity and degree of polarization (DP) across the entire sky, or even in a sweep along a given meridian plane, in a

pure Rayleigh atmosphere? To answer that question it is imperative that a correct relationship be written which will give an unambiguous value of DP. Only in the plane of the sun's vertical (i.e., the plane containing the center of the solar disk, the point of observation and the zenith) is the degree of polarization given by:

$$DP = \frac{I_r - I_l}{I_l + I_r}$$

The sun vertical plane contains more information regarding polarization than any other meridian plane across the sky. Away from the sun's vertical plane, the proper expression for the polarization is:

$$DP = \frac{\sqrt{Q^2 + U^2 + V^2}}{I}$$

As an initial test of our G-S iterations, we show in figure 2 a direct comparison to some graphs transcribed from the work of Coulson (1988), for both high and very low sun elevations. His treatment was an exact one, employing Chandrasekhar's X and Y functions. The agreement of our model with Coulson's calculations is good considering that only a medium-resolution angular grid was used in the initial development of our G-S codes. In all instances in our analyses, the layer optical depth was kept at about $\Delta\tau = 0.02$. For the visible and near-IR wavelengths, the number of layers needed in our model therefore was fairly small (between 5 and 10). In every case, the number of iterations necessary to achieve good convergence was either 3 or 4.

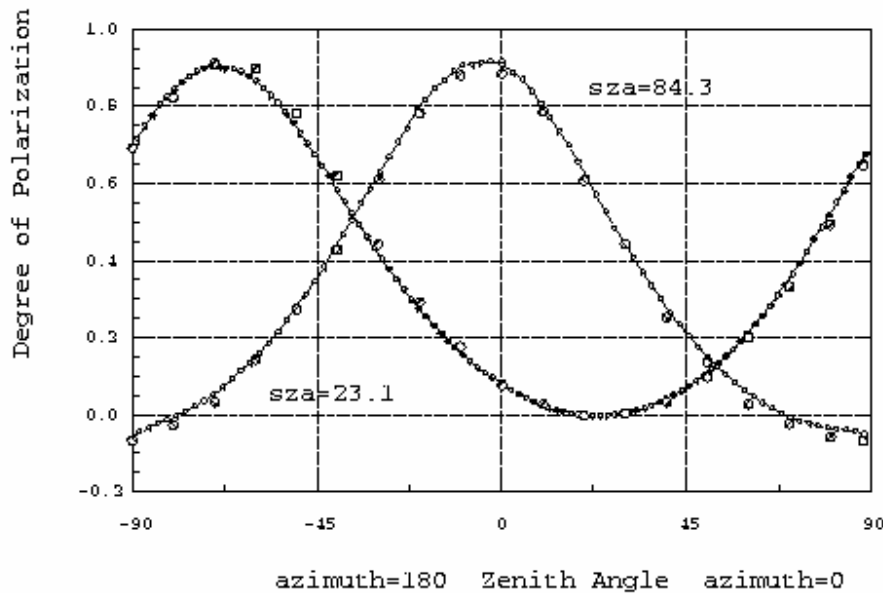


Figure 2. Polarization in the sun's vertical plane for a pure Rayleigh atmosphere. Comparison of DXK Gauss-Seidel model with the calculations of Coulson (circles). Two different solar zenith angles (sza) are indicated.

2.5 Mie Multiple Scattering

Whereas the phase function for scattering in a clean, Rayleigh atmosphere is readily expressed, and is proportional to $\cos^2\theta + 1$, the same thing cannot be said for its aerosol counterpart. Even if the refractive indices, chemical composition, sizes, and number densities of the atmospheric particles were known exactly, the radiative transfer problem for haze and clouds remains very difficult owing to uncertainties in accounting for non-sphericity of the particles and handling their forward scattering diffraction peaks.

Execution of an equivalent version of the Gauss-Seidel routines used for the molecular atmosphere is now performed for a collection of spherical particles. The Mie phase matrix elements are found from interpolation within a subroutine provided by Lacis (1990). Only the elements P_{11}, P_{12}, P_{33} , and P_{34} are needed. These 4 quantities along with 4 other non-zero values obtained from the former, comprise the matrix that operates on (I, Q, U, V) , the Stokes vector itself. When the multiplication is done on (I, I_r, U, V) , the vector used in the Rayleigh multiple scattering procedure, a transformed matrix consisting of only 6 non-zero elements results. Bohren and Huffman(1983) explicitly provide the relationships to go from one system of polarized intensities to the other. The 2 new elements in the (I, I_r, U, V) , system are: $P'_{11} = P_{11} +$

P_{12} and $P'_{22} = P_{11} - P_{12}$. In the new system $P'_{12} = P'_{21} = 0$. With $\tilde{\mathbf{P}}_{\text{Mie}}(\theta)$ thus formed, $\tilde{\mathbf{P}}_{\text{Mie}}(\mu, \mu', \phi, \phi')$ is then found by way of the rotations described previously.

First we need to verify the reliability of our model for a situation with only particles present. A good test case is that presented by Hansen (1971). Using a standard Γ distribution for a collection of liquid water cloud drops having a particle effective radius $a = 6 \mu\text{m}$, variance $b = 0.111$, real part of the refractive index $n_r = 1.29$, and imaginary part $n_i = 3.04 \times 10^{-4}$, we have simulated the polarization of the light reflected from such a cloud, where the total optical depth is 0.25. Normally incident sunlight is assumed (i.e., $\mu_0 = -1.0$). The wavelength is $\lambda = 2.25 \mu\text{m}$. Comparison of our Gauss-Seidel calculated DP values with those from the doubling-adding method of Hansen is made in figure 3.

We can also check to see if our computed intensities for the “particle-only” ensemble are consistent with those determined by an independent method. To do this, we ran a doubling-adding code adapted from Tomasko and Doose (1989). We chose the same wavelength and optical constants that were used in the preceding comparisons to Hansen’s water drop simulations. We selected a particle effective radius equal to the wavelength. In that case there should be very little difference in the retrieved intensities found from a scalar model compared with those from a polarized treatment. We elected to run the full polarization version of our code. figure 4 displays the transmitted intensities in the solar vertical for $\phi = 0^\circ$ obtained with the 2 methods for the specified input.

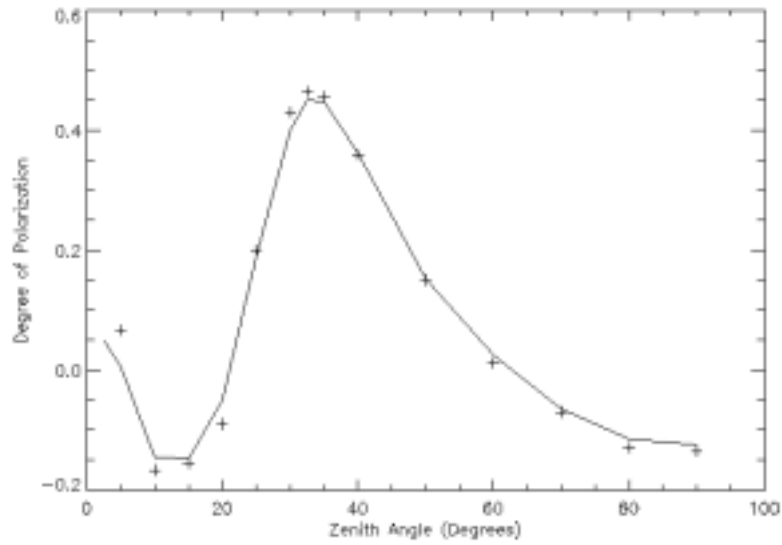


Figure 3. Polarization of near-IR radiation ($\lambda = 2.25 \mu\text{m}$) reflected by a cloud ($\tau = 0.25$) of water drops ($n = 1.29 + 0.000304i$) for perpendicular incidence. Comparison of DXK G-S model (solid curve) with Hansen's doubling-adding method (crosses) using a Standard Γ cloud drop size distribution with $a = 6 \mu\text{m}$ and $b = 0.011$.

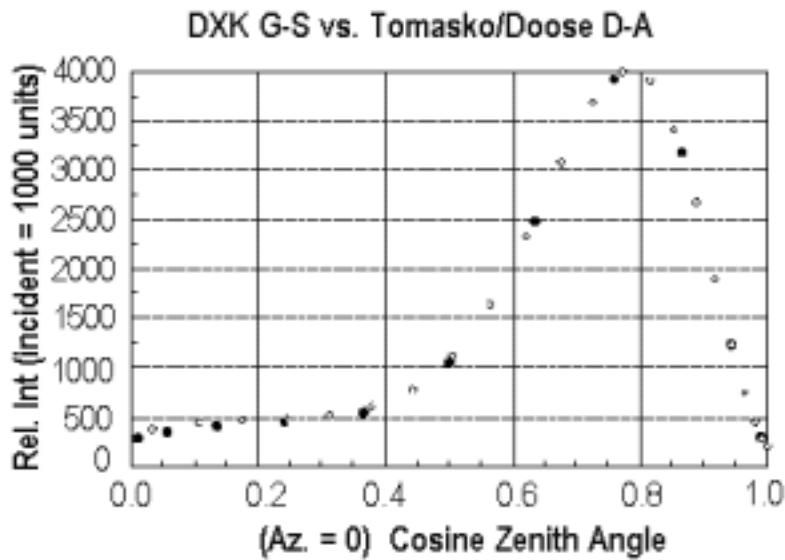


Figure 4. Transmitted intensities in the solar vertical with adaptation of doubling-adding code from Tomasko and Doose (filled dots) versus DXK G-S model (diamonds) using the following input parameters: $\tau_{Mie} = 0.50$, $\lambda = 2.25 \mu\text{m}$, $a = 2.25 \mu\text{m}$, $b = 0.03$ (from standard Γ distribution), $n = 1.29 + 0.000304i$, and $\mu_0 = -0.8$. In the present Gauss-Seidel simulation, 5 iterations were performed using 25 model atmosphere layers.

2.6 Spectral Transmittance through Gases

The mathematical complexities outlined in the foregoing discussion of radiative transfer theory have entailed problems almost exclusively relating to scattering, either by air molecules or by aerosols. In contrast, the basic process of absorption of electromagnetic radiation is not nearly so difficult to incorporate in the solution of the full RTE. Nonetheless, some caveats must be given. Because the spectral variation of absorption coefficients for gaseous constituents is a highly oscillating function of wavelength, an uncritical, inadvertent use of a simple exponential decrease in spectral transmittance with the linear increase of absorber amount will almost certainly lead to an erroneous assessment of the average spectral transmittance through the gas. So often though, for a variety of reasons relating to expediency, just such a naive tack is followed, whereby the simple Lambert law of attenuation, viz., $T_\lambda = \exp(-k_o\lambda u)$ is applied typically to some smoothed value of the molecular absorption coefficient ($k_o\lambda$) and multiplied by the absorber optical path (u). A preferred procedure is to either use a complete line-by-line spectral integration approach, routinely done by numerous workers who tie into databases like HITRAN, or to set up some type of exponential sum fitting of transmittances (ESFT) scheme in order to accomplish the stated task of ascertaining a proper average spectral transmittance. One quite recent example of this latter approach can be found in Appendix 1 taken from Kerola et al. (1997).

2.7 Preliminary Computation of Ozone Optical Depths

As an initial “placeholder” kind of calculation of spectral line optical depths of O₃ to be used in the first phase of the GLI atmosphere correction tasks, use is made of the low-resolution absorption coefficients reported by Leckner (1978) and re-tabulated by Iqbal (1983). Until our Terrestrial Biophysics Remote Sensing Group (TBRS) can fully implement its Science Computing Facility (SCF), hopefully to be accomplished in early 1998, the use of the HITRAN database to calculate ozone transmittances will be precluded owing to its very large size (≈ 0.5 GBytes). Attempts to explore the viability of an ESFT-style procedure will possibly be made at the start of the second period. The dilemma in constructing an ozone-adapted ESFT technique is the requirement that laboratory measurements of O₃ transmittances for a variety of path lengths and relevant wavelengths must be available. It is not clear at this juncture whether those kinds of data can be acquired.

2.8 Use of Full Radiative Transfer Methods to Perform Atmosphere Correction For Satellite Remote Sensing of Earth by the Global Imager (GLI)

- **Basic Picture of Global Atmospheric RT**

figure 5 is a depiction of how we can construe the fundamental problem at hand; namely, how do we envision setting up viable and yet rigorous computational procedures along with associated templates of input data pertinent to atmospheric physical properties (ANC) as well as satellite real-time orbital information (GAC).

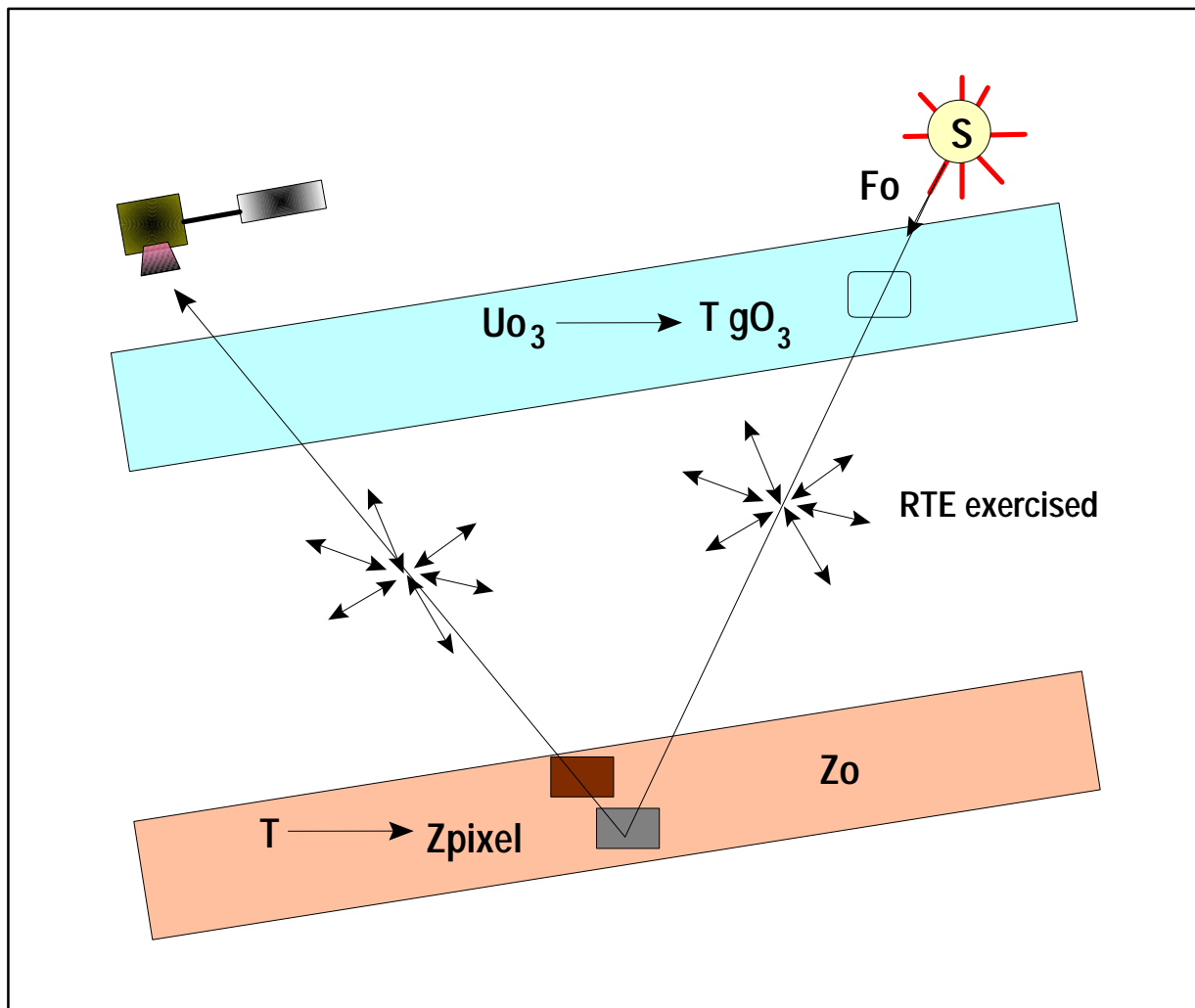


Figure 5. Basic schematic showing the strategy for generating atmospherically-corrected global-scale maps of surface reflectance. In the actual modeling, the 2-way ozone transmittance factor (T_{gO_3}) is applied after the Gauss-Seidel iterations are performed on the "Rayleigh-only" component of the atmosphere.

The plan is tantamount to the placement (e.g. co-georegistration) primarily of 2 distinct input data layers (which together account for both the stratospheric ozone spectral absorption and the altitude adjustment of the magnitude of Rayleigh scattering for the individual pixels in the GAC scenes.

- **Calculation of First-order Surface Reflectances**

In the customary tradition of Earth remote sensing, the spectral radiances obtained by exercising the adopted RT code can be expressed as a bi-directional reflectance, given as:

$$\rho = \frac{I(\tau, \mu_v, \Delta\phi)}{\mu_0 F_0}$$

where the calculated spectral intensity (called radiance typically by the terrestrial community) is a function of the optical depth (τ), the zenith direction of view (μ_v), and the relative azimuth angle between sun and sensor ($\Delta\phi$). In this expression, μ_v is solar zenith direction and F_0 is the input solar radiance. It is to be noted that in all the formulations given in section 2 of this presentation the incident sunlight is expressed explicitly as a radiance *per se*, whereas many of the forms appearing in the literature will use the solar astrophysical flux (given by $\pi * F_0$).

We can proceed then to write a straightforward relationship giving the normalized radiance (ρ^*) measured at the top of the atmosphere (TOA) by the satellite detectors. We have:

$$\rho^* = \rho_a + \rho T^r T_{gO_3}$$

Neglecting the non-linear coupling between the atmosphere and ground, we see that the reflectance of the atmosphere *per se* is ρ_a , the reflectance by the surface is ρ , with T^r and T_{gO_3} being the two-way spectral transmittance functions, respectively, for the Rayleigh component of the atmosphere and for the gaseous component, which, in our initial correction procedures only will entail stratospheric ozone absorption. In terms of the fundamental input parameters in our model, these transmittance functions are:

$$T^r = e^{-\tau_{Ray} \left(\frac{1}{\mu_0} + \frac{1}{\mu_v} \right)}$$

and

$$T_{gO_3} = e^{-\tau_{O_3} \left(\frac{1}{\mu_0} + \frac{1}{\mu_v} \right)}$$

where τ_{Ray} and τ_{O_3} are the Rayleigh scattering and ozone absorption optical depths, respectively. Thus, if we are provided with the TOA calibrated radiance measurements, we can merely make an algebraic rearrangement to derive a first-order estimation of the surface bi-directional reflectance. It would be:

$$\rho = \frac{\rho^* - \rho_a}{T^r T_{gO_3}}$$

2.9 GLI Atmospheric Correction -- Summary of Operational Version of LTSK1 for October 1998 GAIT Algorithm Delivery

- ***Adaptations of LTSK1 for SeaWiFS simulations and for GLI specific use:***

Work toward that end has been appropriately aimed at simulations using SeaWiFS, whose central wavelengths and spectral bandwidths for its 8 visible and near-IR channels match fairly closely GLI channels 3,4,6, 7,9,13,17, and 19. Information from the SeaWiFS GAC HDF data sets needed by both the atmospheric correction and MVC codes were ingested into the processing programs. A fortran routine named "Process.f", which calls a C routine, was designed for reading and writing a 14 parameter per-pixel binary data structure consisting of the 8 SeaWiFS TOA radiances, 3 angles used directly by the radiative transfer code to calculate the intensity of the scattered light, pixel latitude and longitude, and the day of the year information. To begin our analyses on GLI synthetic data (GSD), we augment the dimensions of that input buffer array to 15 in order to accommodate a ninth GLI spectral channel.

The next step has been to adapt a subroutine, which consists of a modified version of LTSK1.F, to work in conjunction with the program "Process.f" . That main routine calls the modified LTSK1 in order to perform atmospheric correction via interpolation on pre-stored look-up tables of the atmosphere per se reflectances for each of the 8 wavelengths commensurate with the SeaWiFS spectral channels. For the GLI-specific operational atmospheric correction algorithm we have prepared 18 distinct lookup tables (LUTs) for the pertinent central wavelengths of the GLI visible and near IR channels 1,5,8,9,13,15,17,19,24,26,28 and 29 to be used by the Land Group. All of these channels are at 1km resolution). So, for executing the operational processing program , we use the 12 GLI-specific wavelengths and LUTs'.

As a preliminary offering of our test results, we prepared for display purposes an uncorrected SeaWiFS Level 1-A Red-Green-Blue (RGB) image for a large subsection lying over the southwest United States (figure 6a). We have also made an ENVI-generated image of that entire region after atmospheric correction (figure 6b). In these displays, Red corresponds to SeaWiFS spectral band 8, Green to band 6, and Blue to band 2. For this single-day test data (day 302), we make use of that day's gridded average global (1 by 1.25 degree) TOMS ozone path lengths. For purposes of making the adjustments for the effects of Rayleigh, polarized multiple scattering as a function of pixel elevations, a full global coverage ETOPO5 elevation grid was laid down. Note that as of June 2001, the whole atmospheric correction code has been converted to ANSI C with HDF file input/Output for better performance.

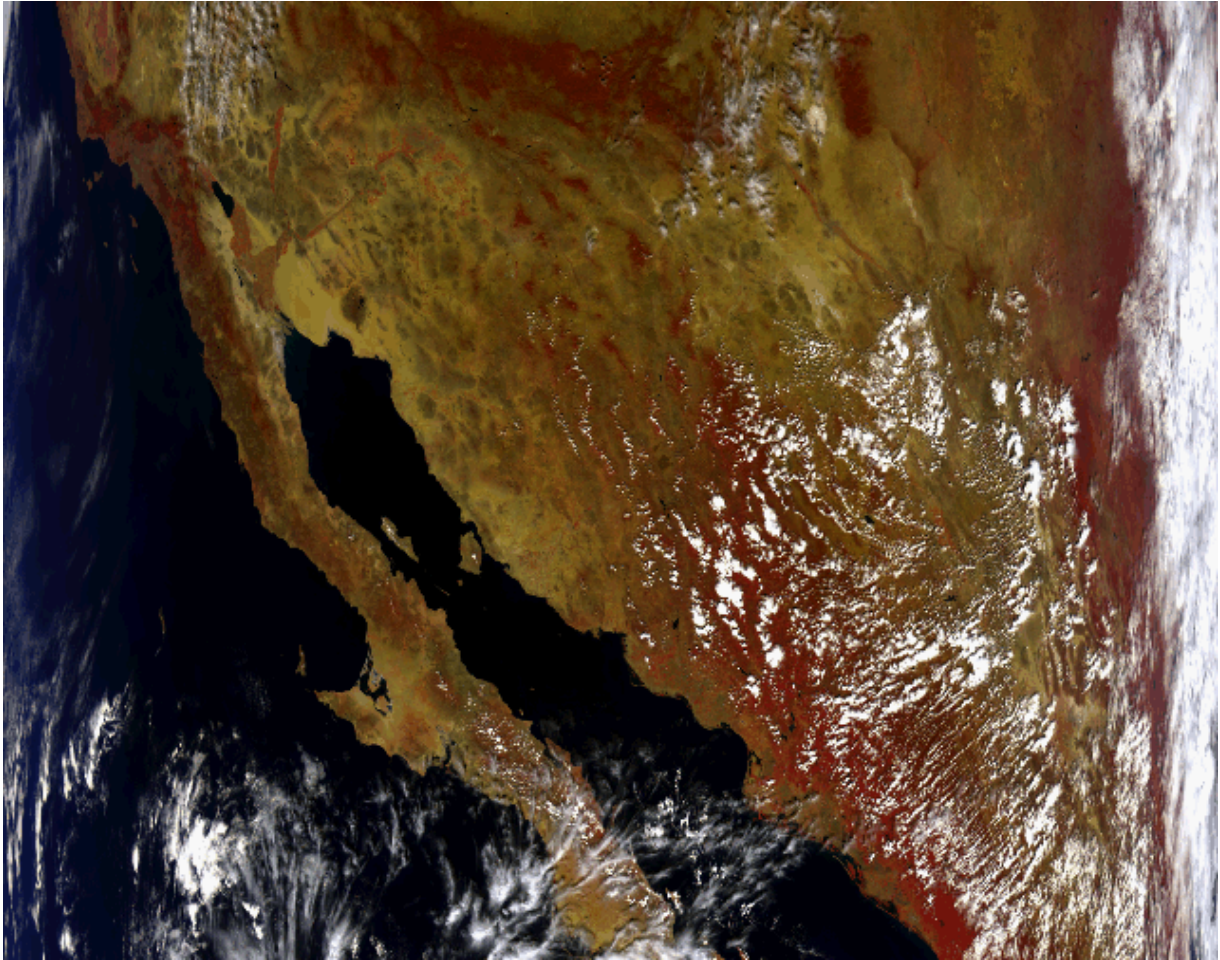


Figure 6a. SeaWiFS raw Level 1-A radiance-count RGB image (with bands 8,6,and 2) for local area coverage (LAC) 1-km data taken from October 28, 1997 over the southwestern United States and Mexico.

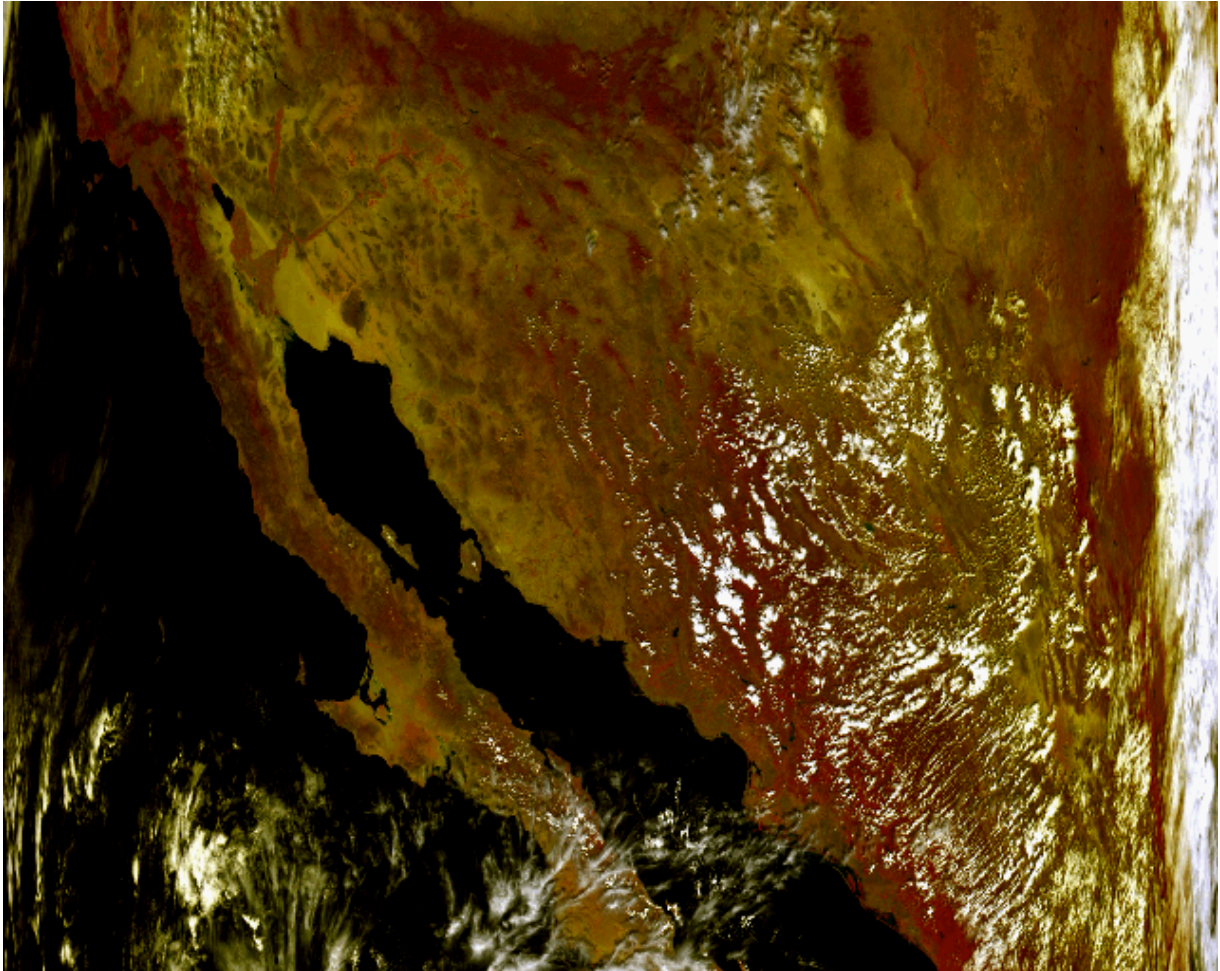


Figure 6b. Rayleigh plus ozone atmospherically corrected RGB reflectances of the October 28, 1997 SeaWiFS LAC scene.

- ***Justification of our adopted computational approaches***

Although many might argue with the need for incorporating such rigorous, often very computationally burdensome, procedures for determination of the atmospherically scattered sunlight, it is quite possible nonetheless that the inclusion of a vectorized treatment (i.e., with polarization taken into account) could yield dividends. In the rapidly advancing era we are in, where the capacity and speed of even desktop computers permit the calculation of the complete phase matrices used to determine both the intensity and state of polarization of multiply-scattered

light, it is advantageous to embody as close to complete a treatment of the radiative transfer problem as possible. For that matter, already a decade ago, workers like Gordon et al. (1988) saw such a reason to compute the full-up Stokes parameters. They were applying their own atmospheric correction schemes to the analysis of spectral data coming from the Nimbus-7 Coastal Zone Color Scanner (CZCS), which was the precursor to what we are now adopting in our 1998 simulations, namely, the Sea-Viewing Wide-Field Sensor (SeaWiFS).

- ***Assessment of Expected Accuracy and Intrinsic Uncertainties in our Adopted Radiative Transfer Code***

A) Verification of our Algorithms

In the GLI Interim Final Report (Dec. 1997), we showed several examples of how closely our Gauss-Seidel vectorial computations match the results produced from other comparable codes. It is often very difficult to find enough detailed summaries of calculations performed in the past for which the previous workers provide clear-cut specification of their input quantities. Whenever we have been able to make some unambiguous one-to-one correspondences of input parameters (e.g. against the work for cloud droplets by Hansen (1971) and for the Rayleigh polarized atmosphere against the Monte Carlo calculations of Marchuk (1980), we have found that our techniques yield results that are consistently between 1 and 2 percent of their simulations in the longer wavelength regions of the visible spectrum, i.e., for yellow through red light. When we go to shorter wavelengths, i.e., for blue light, our simple numerical integration of the azimuthal angular component of the multiply scattered light results in a non-conservation of radiative flux, thereby causing deviations in our modeling of several percent compared with more traditional approaches which use spherical harmonic functional expansions to get the azimuthal contribution to the multiply scattered light. In addition, our present version of the operational code has a bi-linear interpolation scheme which might be causing an underestimation of the corrected surface reflectances in the blue channels of several percent, compared with a what a bi-cubic type of interpolation is expected to give.

To demonstrate the fundamentally sound behavior of our atmospheric correction techniques, we can show a plot of the spectral signatures for individual pixels not contaminated by cloudiness in a test run using 4 km SeaWiFS GAC data over Thailand. For instance,

isolating on pixel number 214 along the first scan-line of our chosen scene, we plot (figure 7) the pre and post-corrected spectral surface reflectances across the wavelengths spanned in the SeaWiFS solar channels. The before and after trends do indeed meet expectations. The code appears to be doing a fairly good job in correcting at the blue end of the spectrum the sizeable effects of Rayleigh multiple scattering., thereby leaving only minimal vestiges (only about 0.01) for the surface reflectance at about 450 nm. The particular pixel selected for this illustration is located at 21.106 N. latitude and 104.124 E. longitude, about 2 degrees west of Hanoi, Vietnam. We see the low values of the reflectances well into the red portion of the spectrum, with the significantly elevated values as we reach the near-IR, so characteristic of healthy green vegetation.

One other kind of presentation which is instructive in highlighting how well our methods are in place, is to show the post-atmosphere corrected spectral signatures for a few uncontaminated pixels across a fairly representative and diverse span of an IDL-derived TV image over southeast Asia with the SeaWiFS GAC data. Along the lines of what has been reported recently, e.g., by Huete et al. (1997), we present in figure dxk4oct spectral signature curves targeting 4 distinct land cover types. Our results replicate the overall characteristic slopes and spectral reflectance magnitudes derived in the Huete et al. (1997) work.

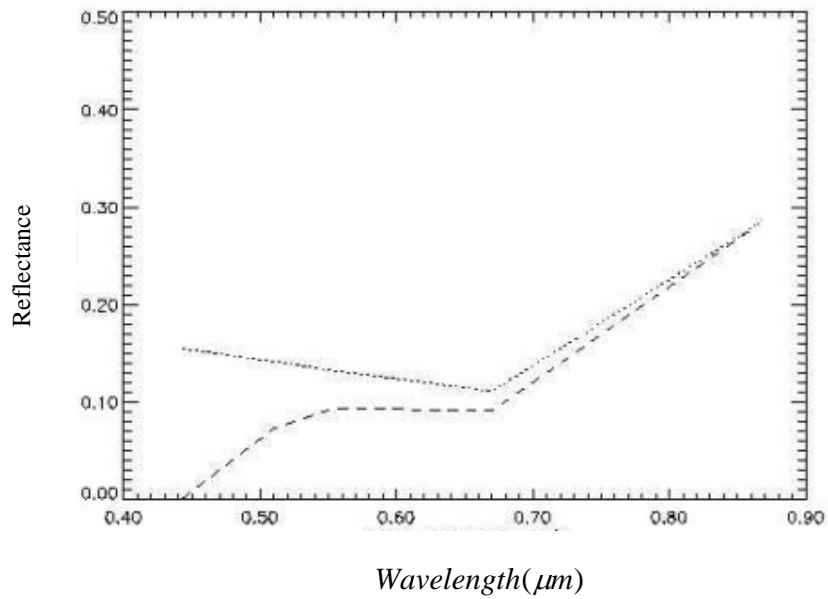


Figure 7. Depiction of typical per pixel spectral reflectances from the SeaWiFS 1997 day 259 4-km GAC analysis over southeast Asia. The plot gives the observed TOA reflectances (dotted) and the Gauss-Seidel interpolated Rayleigh plus ozone corrected surface reflectances (dashed).

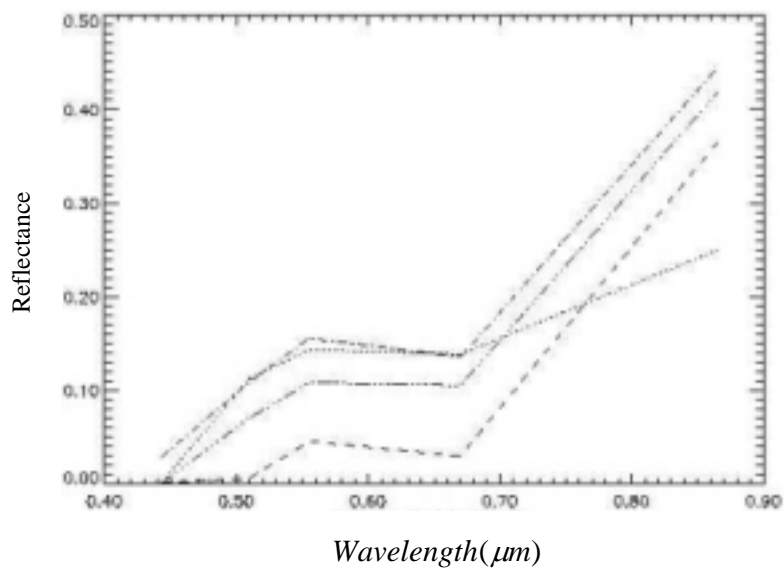


Figure 8. Corrected reflectances for individual pixels in the SeaWiFS day 259 GAC analysis. The locations are : (1) 22.648 N., 90.854 E. (dotted), (2) 22.543, 92.423 (dashed), (3) 21.98.196 (dot-dash), and (4) 19.574, 100.079 (triple dot-dash). These target pixels represent areas lying (1) near Bharpara, India, (2) in southern Bangladesh, (3) southeast of Mandalay, Burma, and (4) in north-central Thailand.

B) Toward Validation of SeaWiFS-Derived Top-of-Atmosphere (TOA) Radiances

The next step for us to demonstrate the soundness of both our science and operational processing codes, will be the reconciliation of actual satellite TOA radiances with those inferred from actual field measurements aimed at establishing "ground truth". The TBRS group has substantial experience in conducting a variety of field validation studies across numerous terrains in the United States and elsewhere. The difficulties are probably just as great in trying to achieve a true validation of observed satellite measurements as they are in trying to intercompare different radiative transfer codes (as described in the previous section). At this stage in our progress, we must rely on some prior extensive work in the area of vicarious calibration (cf. e.g., Thome, et al. 1993).

C) GLI Atmospheric Correction performed on MODIS data

To assess the performance of the LTSK1 code compared with the current MODIS atmospheric correction algorithm, a test was performed with 1km MODIS data over Japan. A granule (2030 x 1354) of MODIS L1B level data was acquired as radiances (DOY272, Year 2000). The GLI atmospheric correction code was ran for a single day using three bands (Red, Nir and Blue). figure 9 and figure 10 show respectively a false color composite of a MODIS L1B atmospherically corrected image using LTSK1 and the corresponding image atmospherically corrected by the MODIS algorithm. Since the MODIS and the GLI bandpasses are not the same we don't expect very reliable results. In the future, we plan on performing more rigorous comparisons between the GLI algorithm and the MODIS atmospheric correction code which was proved to be robust and reliable.

D) Practical Considerations

In this section we shall explore some of the proposed algorithms aspects with respect to implementation, programming and data exchange.

(1) Programming, Procedural, Running Considerations

Development of An Operational Processing System for GLI

1.1 Creation of Prototype Algorithms for Performing Atmosphere Correction

The first steps in creating a mechanism for doing atmosphere correction on the GLI-specific GAC and ANC input data involve (1) exercising the full RT code for likely solar and

view geometries, global ozone amounts, and global land elevations, and then (2) storing the results from step (1) in sets of look-up tables for use in an interpolation routine designed to be a prototype module for a pixel-by-pixel calculation of expected atmosphere reflectances. The philosophy behind the construction of the “look-up table” approach is somewhat reminiscent of that done by Fraser et al. (1992). In that work, interpolation was performed over various wavelengths and aerosol optical depths. In addition their program was designed (as our present code is too) for accommodation of a range of μ_0 , μ_v , $\Delta\phi$, z , and u_{03} values as well. The work we are undertaking during this first phase in the GLI project is restricted to an ozone plus Rayleigh correction only. As of November, 1997 our prototyping efforts along these lines have progressed to a point where we can demonstrate its speed and efficacy in computation of ρ_a values for arbitrarily supplied individual values of sun angle and view angles on spatial scales as fine as roughly 1 square kilometer using available GTOPO30 digital elevation information.

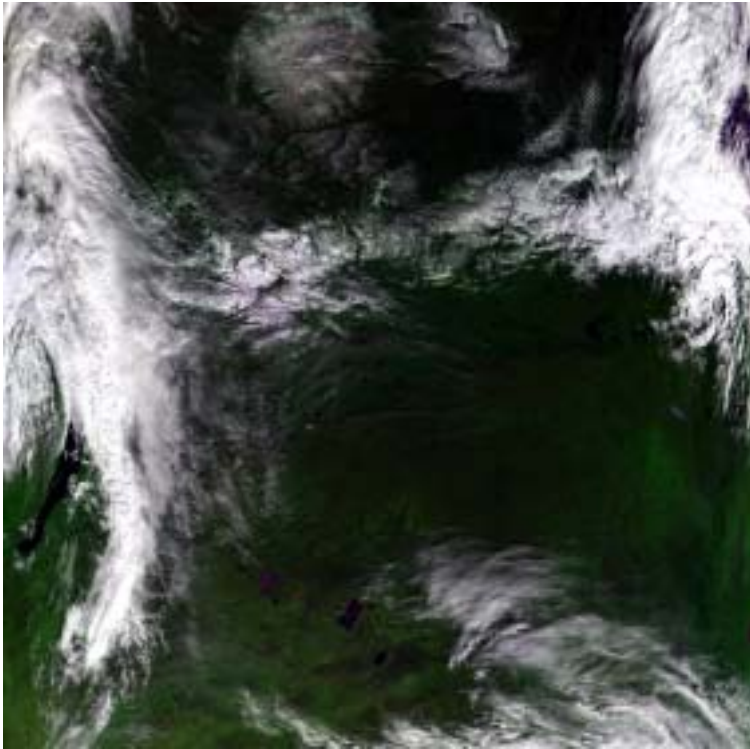


*Figure 9: False color composite
GLI atmospheric correction
algorithm performed on Modis LIB
data*

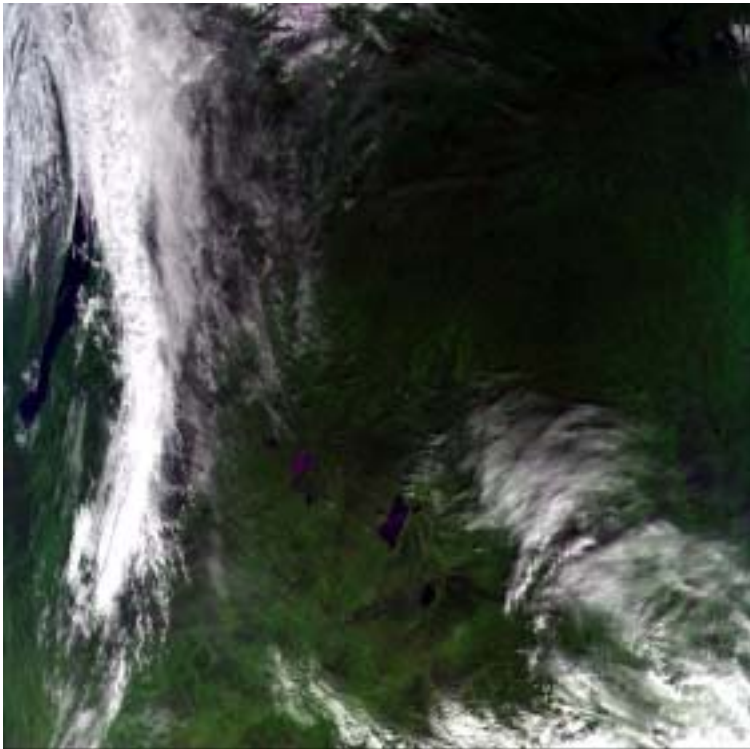


*Figure 10: Modis Equivalent
Surface Reflectance product
MOD09 for the same day*

1.2 Research Progress Through The First Period: GLI Atmosphere Correction

Elements of Proposed Procedures

STEP 1

Generation Of Wavelength-Distinct Look-Up Tables For Use In GLI Global Scale Ozone Plus Rayleigh Atmospheric Correction

Execution of polarized multiple scattering code (DXK G-S) for the following “bracketing” input quantities:

- solar zenith cosines μ_0 : -0.25,-0.30,-0.40,-0.50,0.60,-0.70,-0.80,-0.90,-0.998
- ozone optical paths u_{O_3} (cm-atm): 0.280, 0.300, 0.3125, 0.325, 0.337, 0.340, 0.350, 0.360, 0.375, 0.390
- surface elevations z (meters) -600.0,0.0,600.0,1200.0, 1800.0,2400.0,3000.0, 3600.0,4200.0,4800.0,5400.0,6000.0,6600.0,7200.0, 7800.0, 8400.0,9000.0
- Storage of atmosphere reflectance(ρ_a) output grids; each grid consists of ρ_a values at 6 ρ_v and 12 (ϕ_0 - ϕ_v) points. The “lookup-table” is a sequential set of grids. The total number of grids stored in the output file (per wavelength) is the product of the dimensions of the input arrays.

STEP 2

I-O Flow In Ongoing Development Of GLI Operational Processing System

Results from STEP 1 are now fed selectively to another program which is designed to perform the required interpolation of the ρ_a values on a pixel-by-pixel basis using a global area coverage (GAC) and ancillary (ANC) input data flow shown in figure 11. Prototype tests using this processing scheme have already been performed with a limited subset of actual ANC data.

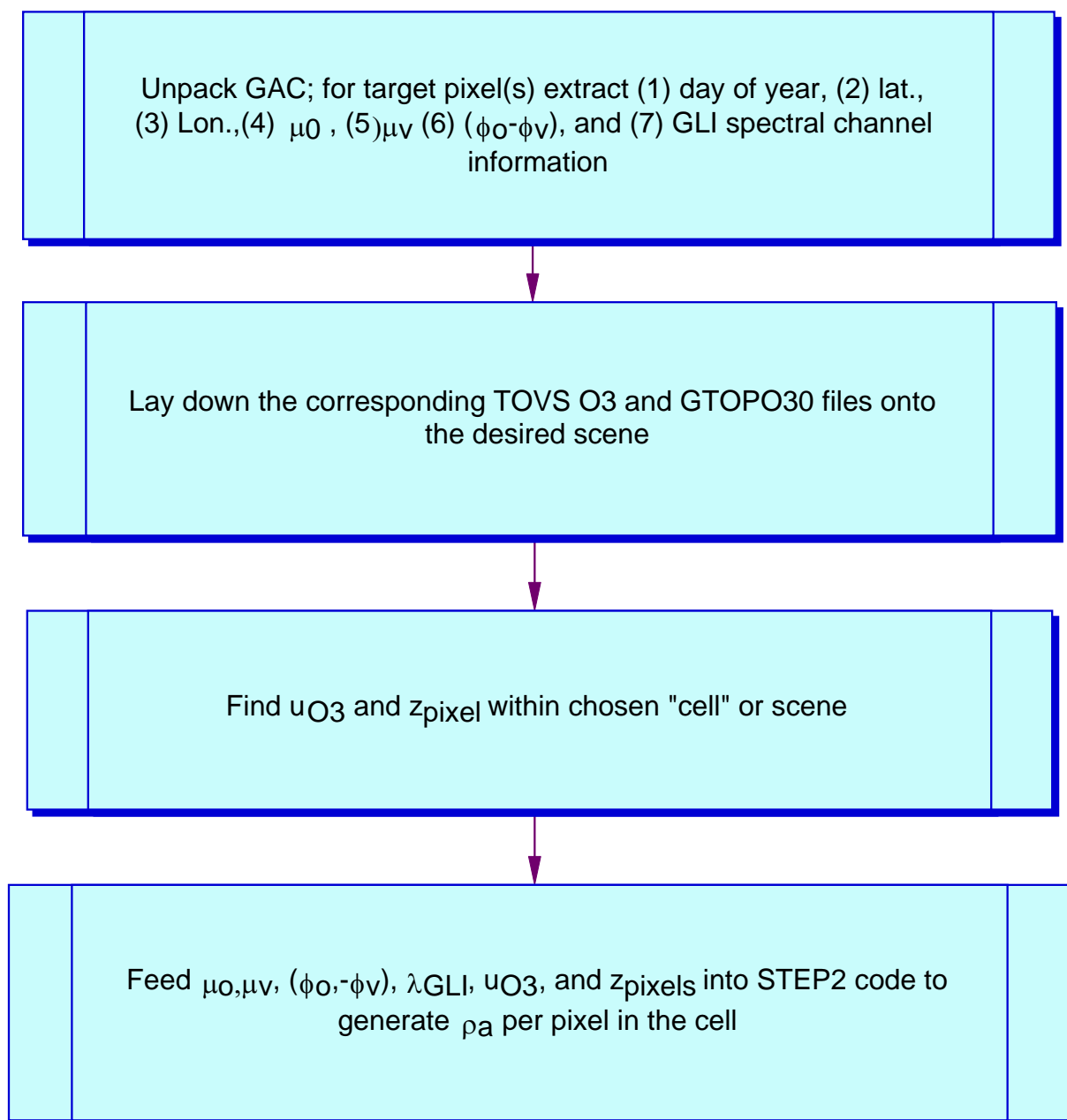


Figure 11: Basic Flow chart of requisite input data to permit computation of the ozone plus Rayleigh atmospheric reflectances.

1.3 Ancillary Data Acquisition and Data Formats

The most challenging aspect of implementing an accurate, efficient atmospheric correction plan for use in generating global scale products will center on how best to acquire, store, convert, and structure the “input-output” (I/O) data streams at various intermediate stages in the project. With the advent of our TBRS SCF there should be encouraging progress soon on that front. Already, because of the rapid pace at which various U.S. Federal organizations are

making their datasets available through the Internet, a great deal of manageably-sized files can be used directly in our ongoing prototyping efforts. For example, through a NASA GSFC web site Nimbus-7 TOMS ozone data is available for the entire globe as 1° daily or monthly gridded averages. These data can be secured via ftp in IEEE binary file format. In addition, through NOAA's National Geophysical Data Center, global DEM terrain data are available also by ftp for user-specified geographic regions (cf. <http://www.ngdc.noaa/mgg/global/global.html>). Furthermore, much of this kind of data (i.e., ETOPO5 cells) is produced for instant downloading in ASCII format.

1.4 Prototype Atmosphere Correction: Analysis Example

As a quick trial of our rudimentary code, we turn to the 2 web sites cited above for some sample test TOMS O₃ and ETOPO5 elevation data. We arbitrarily select a sample of monthly mean ozone data from Nimbus-7 TOMS measurements in April, 1993. We acquired 2 adjacent 1 by 1 degree ETOPO5 cells which give surface elevations (in meters) for a region in southern Arizona stretching from latitude +33.0, longitude -112.0 on the northwest, to latitude +32.0, longitude -111.0 on the southeast. Then the RT interpolation program was executed for $\lambda = 825$ nm (GLI channel 23), $\mu_0 = 0.95$, $\mu_v = 0.75$, and $\Delta\phi = 390.0^\circ$. An adjustable spatial resolution parameter can be fed into the included ETOPO5 cell data, allowing a bi-cubic interpolation over ground heights to a scale as fine as about 50 arc secs. Any desired resolution better than this would probably begin losing accuracy. Soon to be released higher resolution DEM Global data sets should permit the ≈ 10 arc sec (≈ 0.25 km by 0.25 km on the ground) resolution we are ultimately trying to achieve. In figure 12 we show an IDL-produced TV image of this particular simulation (for 100 arc sec individual pixel scale) of the intrinsic atmosphere reflectance for the chosen scene. The range of reflectance across the image corresponds to $\Delta\rho_a = 0.012 - 0.014$.

In order to improve the accuracy of the atmospheric correction code, some changes have been made for the ancillary data. The Ozone data is now obtained from the Tiros Operational Vertical Sounder system (TOVS), flown on the NOAA Operational Polar Orbiting Satellite series while the elevation data is obtained from the Global 30 Arc Second Elevation Data Set (GTOPO30) available at the USGS web site. figure 12 shows an example of such data set. Since the GLI Projection Grid and GTOPO30 are both static, the ingestion of the GTOPO30 dataset requires generating GTOPO30 tiles to match the GLI tiles on a pixel basis. Such operation results in the generation of 56 tiles. figure 13 shows an example of GTOPO30 GLI Tile for the South Pole.

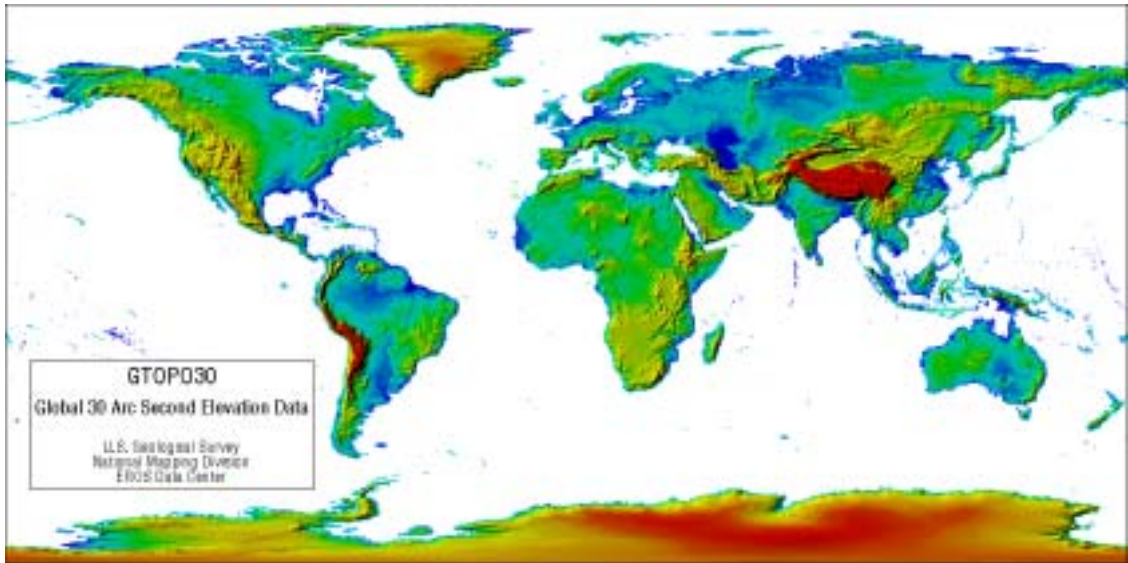


Figure 12: GTOPO30 dataset

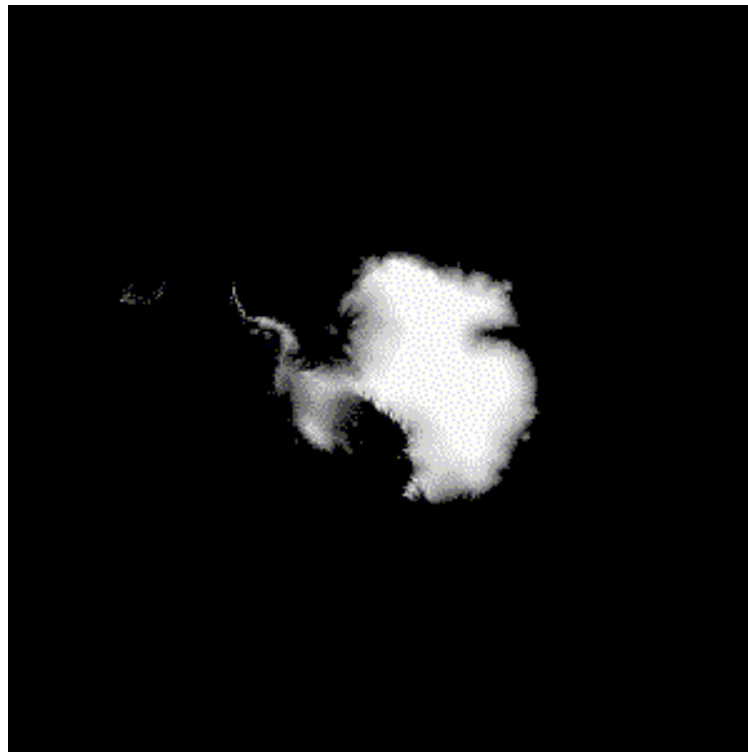


Figure 13: Example of GTOPO30 GLI Tile for the South Pole



Figure 14. DXK G-S model simulation of atmosphere reflectance (corrected for Rayleigh scattering and ozone absorption only) in south-central Arizona. The geographic test grid extends from lat.= +33.0, lon.= -112.0 to lat.=+32.0, lon.= -111.0. The test was arbitrarily run using Nimbus-7 TOMS monthly averaged ozone amounts for April, 1993. The ETOPO5 dataset was downloaded directly in ASCII format from the website listed in the text. The range of reflectance in the frame is 0.010 to 0.014.

(2) Calibration and Validation

(3) Quality Control and Diagnostic Information:

The algorithm will include a portion dealing with Quality Assurance (QA) issues. The goal of the QA is to guarantee a better data quality and consistency both spatially and temporally. Inconsistent products may depict spatial and temporal variations in their values unrelated to Earth's surface states and processes. In order to prevent such data consistency problems and poor data quality of that kind, it is necessary to develop such an algorithm. The GLI atmospheric correction will have a built-in QA/QC routine to warrant the data quality. figure 15 shows an example of such a QA/QC product.

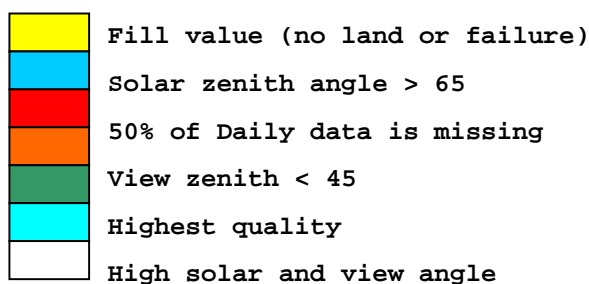
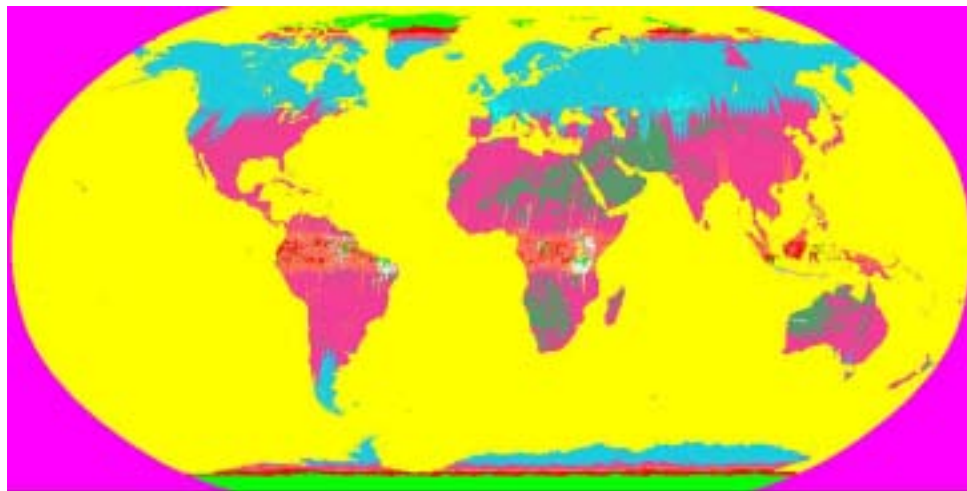


Figure 15: Example of QA/QC map for GLI

(4) Exception Handling

Exception handling is the technique adopted to account for unforeseen situations. Missing data, missing ancillary data, sensor behavior, floating point error during computation, data out of

range and so on. In a generic approach, any time the algorithm does not perform as designed, the data will generate an exception handler. However, during the run the algorithm will use a generic success flag to track the execution of the different parts. Anytime an exception handler is generated the pixel value will not be updated (VI's case) and most probably a pre-determined value (-300, -2000) will be appended instead. When the atmospheric correction algorithm fails a scheme was designed that consists of using a set of fill values generated before the compositing takes place.

(5) Constraints, Limitations, Assumptions

As proposed in phase one, the atmospheric correction will only be concerned with Rayleigh and Ozone. Two major shortcomings are noted here:

- 1) No account for BRDF and
- 2) Not account for water vapor (an empirical approach will be implemented).

For the time being we advise that aerosol correction should be applied at a later stage and on a per demand basis. The BRDF product, by which data will be normalized to "*nadir*" view angles could be adopted if research, and funding permits.

(6) Suggestions and Recommendations

We will be looking into the feasibility, should the need arise, of extending the radiative transfer methods described in this ATBD in order to potentially accommodate calculations of aerosol scattering (based plausibly upon current climatological models of tropospheric and stratospheric haze geographic and altitudinal distributions) and water vapor absorption in the visible and near-IR. Incorporation of the latter effect into our present code would follow the lines we have discussed regarding our treatment of ozone discussed elsewhere in this report. A full-fledged treatment on a global scale of the extinction of sunlight by small airborne particles is of course tremendously more difficult to achieve. It's important to realize at this stage, that correction for aerosol is being applied by the ocean group, and we are identifying means of coordinating our work. The data flow-diagram proposed by GAIT and limitations in resources will make some of these tasks hard to apply. Overall, we are confident in the current status of our research, and hope to extend the GLI contribution to the remote sensing community by devising better and sounder techniques for data production.

D. References

- Ackerman, S., K. Strabala, P. Menzies, R. Frey, C. Moeller, L. Gumley, B. Baum, C. Schaaf, G. Riggs, R. Welch, 1996. Discriminating Clear-sky from Cloud with Modis Algorithm Theoretical Basis Document V3, <http://eospsso.gsfc.nasa.gov/atbd/modistables.html>.
- Agbu, P.A., and James, M.E., 1994. The NOAA/NASA Pathfinder AVHRR Land Data Set User's Manual. Goddard Distributed Active Archive Center, NASA, Goddard Space Flight Center, Greenbelt.
- Asano, S. and Uchiyama, A. (1987), Application of an extended ESFT method to calculation of solar heating rates by water vapor absorption, *J. Quant. Spectrosc. Radiat. Transfer*, 38. 147-158.
- Asrar, G., Fuchs, M., Kanemasu, E.T. and Hatfield, J.L., 1984, Estimating absorbed photosynthetic radiation and leaf area index from spectral reflectance in wheat, *Agron. J.*, 76:300—306.
- Asrar, G., Myneni, R.B., and Choudhury, B.J., 1992, Spatial heterogeneity in vegetation canopies and remote sensing of absorbed photosynthetically active radiation: a modeling study. *Remote Sens. Environ.* 41:85-101.
- Baret, F., and Guyot, G., 1991. Potentials and limits of vegetation indices for LAI and APAR assessment. *Remote Sens. Environ.* 35: 161-173.
- Bohren, C.F. and Huffman, D.R. (1983), *Absorption and Scattering of Light by Small Particles*, Wiley-Interscience, New York.
- Chandrasekhar, S. (1960), *Radiative Transfer*, Dover, New York. Coulson, K.L., (1988) *Polarization and Intensity of Light in the Atmosphere*, A. Deepak, Hampton, Virginia.
- Choudhury, B.J., 1987, Relationships between vegetation indices, radiation absorption, and net photosynthesis evaluated by a sensitivity analysis, *Remote Sens. Environ.* 22:209-233.
- Cihlar, J., Manak, D., and D'Iorio, M., 1994b. Evaluation of Compositing Algorithms for AVHRR Data over Land. *IEEE Trans. Geosc. Remote Sens.*, 32:427-437.
- Cihlar, J., Manak, D., and Voisin, N., 1994a. AVHRR Bidirectional Reflectance Effects and Compositing. *Remote Sens. Environ.*, 48:77-88
- Cihlar, J.C., H. Ly, Z. Li, J. Chen, H. Pokrant, and F. Huang, 1997. Multitemporal, Multichannel AVHRR data sets for Land Biosphere Studies— Artifacts and Corrections. *Remote Sens. Environ.* 60:35-57.
- Deering, D.W. and Eck, T.E., 1987. Atmospheric optical depth effects on angular anisotropy of plant canopy reflectance. *Int. J. Remote Sensing*, 8(6), 893-916.
- Deering, D.W. and Leone, 1986. A sphere-scanning radiometer for rapid directional measurements of sky and ground radiance, *Remote Sens. Environ.*, 19:1-24.
- Eidenshink, J.C. and Faundeen, J.L., 1994, "The 1km AVHRR global land data set: first stages in implementation," *Int. J. Remote Sensing*, 15(17), pp. 3443-3462.

- Fung, Y., Tucker, C.J. and Prentice, K.C., 1987. Application of Advanced Very High Resolution Radiometer Vegetation Index to Study Atmosphere-Biosphere Exchange of CO₂. *J. Geoph. Res.*, 92, 2999-3015.
- Giver, L.P., Benner, D.C., Tomasko, M.G., Fink, U. and Kerola, D.X.(1990), Gaussian quadrature exponential sum modeling of near infrared methane laboratory spectra obtained at temperatures from 106 to 297 K.,in First International Conference on Laboratory Research for Planetary Atmospheres, pp. 147-156. NASA CP 3077.
- Goody, R.M. and Yung, Y.L. (1989), *Atmospheric Radiation: Theoretical Basis*, Second Edition, Oxford University Press, New York.
- Gordon, H.R., Brown, J.W., and Evans, R. H. (1988), Exact Rayleigh scattering calculations for use with the Nimbus-7 Coastal Zone Color Scanner, *Applied Optics*, 27, 862-871.
- Goward, D.G., Turner, S., Dye, D.G., and Liang, J., 1994. University of Maryland improved Global Vegetation Index. *Int. J. Remote Sensing*, 15(17), 3365-3395.
- Goward, S.N. Dye, D.G., Turner, S., and Yang, J., 1993. Objective assessment of the NOAA global vegetation index data product. *Int. J. Remote Sensing*, 14, 3365-3394.
- Goward, S.N., and Huemmrich, K.F., 1992, Vegetation canopy PAR absorptance and the normalized difference vegetation index: an assessment using the SAIL model, *Remote Sens. Environ.* 39:119-140.
- Goward, S.N., B. Markham, D.G. Dye, W. Dulaney, J. Yang, 1991, "Normalized difference vegetation index measurements from the Advanced Very High Resolution Radiometer", *Remote Sens. Environ.*, 35:257-277.
- Gutman, G.G., 1991, Vegetation indices from AVHRR: an update and future prospect, *Remote Sens. Environ.*, 35:121-136.
- Hansen, J.E. (1971), Multiple scattering of polarized light in planetary atmospheres. Part II. Sunlight reflected by terrestrial water clouds, *J. Atmos. Sci.*, 28, 1400-1426.
- Hansen, J.E. and Travis, L.D. (1974), Light scattering in planetary atmospheres, *Space Sci. Rev.*, 16, 527-610.
- Herman, B.M. and Browning, S.R. (1965), A numerical solution to the equation of radiative transfer, *J. Atmos. Sci.*, 22, 559-566.
- Holben, B.N. 1986. Characterization of maximum value composites from temporal AVHRR data. *Int. J. Remote Sensing*, 7:1417-1434.
- Huete, A.R. ,1988, A soil adjusted vegetation index (SAVI), *Remote Sens. Environ.* 25:295-309.
- Huete, A.R., Justice, C.O., van Leeuwen, W.J.D., 1996. "MODIS vegetation Index, Algorithm Theoretical Basis Document," <http://eospsso.gsfc.nasa.gov/atbd/modistables.html>.
- Huete, A.R., Liu, H.Q., Batchily, K., and van Leeuwen, W., 1997, A comparison of vegetation indices over a global set of TM images for EOS-MODIS, *Remote Sens. Environ.*, 59:440-451.
- Iqbal, M. (1983), *Introduction to Solar Radiation*, Academic Press, New York.

- James, M.D., and Kalluri, S.N.V. (1994), The Pathfinder AVHRR land data set: An improved coarse resolution data set for terrestrial monitoring, *Int. J. Remote Sensing*, 15(17):3347-3363.
- Justice, C.O., Townshend, J.R.G., Holben, B.N. and Tucker, C.J., 1985, "Analysis of the phenology of global vegetation using meteorological satellite data", *Int. J. Remote Sensing*, 6:1271-1318.
- Kaufman, Y.J. and Tanré, D., 1992, Atmospherically resistant vegetation index (ARVI) for EOS-MODIS, *IEEE Trans. Geosci. Remote Sensing*, 30:261-270.
- Kerola, D. X. (1994), Near-Infrared Spectroscopic Studies of the Troposphere of Saturn, Ph.D. Dissertation The University of Arizona.
- Kerola, D. X. (1996), Polarization and intensity of sunlight in the Earth's atmosphere: revisiting the Gauss-Seidel modeling approach, *Bull. Amer. Astron. Soc.*, 28, 1158.
- Kerola, D. X., Larson, H. P., and Tomasko, M. G. (1997), Analysis of the near-IR spectrum of Saturn: a comprehensive radiative transfer model of its middle and upper troposphere, *Icarus*, 127, 190-212.
- Kimes, D.S., Holben, B.N., Tucker, C.J., and Newcomb, W.W., 1984. Optimal directional view angles for remote-sensing missions. *Int. J. Remote Sensing* 5(6), 887-908.
- Kimes, D.S., Newcomb, N.W., Tucker, C.J., Zonneveld, I.S., Van Wijngaarden, W. De Leeuw, J. and Epema, G.F. (1985), Directional reflectance factor distributions for cover types of northern Africa, *Remote Sens. Environ.*, 17, 1-19.
- Kimes, D.S., Newcomb, W.W., Tucker, C.J., Zonneveld, I.S., Van Wijngaarden, W., De Leeuw, J., and Epema, G.F., 1985. Directional Reflectance Factor Distribution for Cover Types of Northern Africa. *Remote Sens. Environ.* 18:1-19.
- Kuchler, A.W., 1995. Natural vegetation map, In: Rand McNally Goode's World Atlas; 19th edition. Eds. Espenshade E.B. Hudson, J.C., Morrison, J.L.. p 18-19.
- Lacis, A. (1990), private communication. Leckner, B. (1978), The spectral distribution of solar radiation at the earth's surface - elements of a model, *Solar Energy*, 20(2), 143-150.
- Leeuwen van, W.J.D. A.R. Huete, S. Jia, C.L. Walthall, 1996. Comparison of Vegetation Index Compositing Scenarios: BRDF Versus Maximum VI Approaches. *IEEE- IGARSS'96*, Lincoln Nebraska, Vol.3, 1423-1425.
- Leeuwen van, W.J.D., A.R. Huete, J. Duncan, J. Franklin, 1994. Radiative transfer in shrub savanna sites in Niger -- preliminary results from HAPEX-II-Sahel: 3. Optical dynamics and vegetation index sensitivity to biomass and plant cover. *Agricultural and Forest Meteorology* 69, 267-288.
- Leeuwen van, W.J.D., A.R. Huete., K. Didan and T. Laing, 1997a. Modeling bi-directional reflectance factors for different land cover types and surface components to standardize vegetation indices. 7th Int. Symp. Phys. Measurements and Signatures in Remote Sensing, Courcheval. (pp 1-8; in press)

- Leeuwen van, W.J.D., Trevor W. Laing, and Alfredo R. Huete, 1997b. Quality Assurance of Global Vegetation Index Compositing Algorithms Using AVHRR Data. IEEE- IGARSS'97, Singapore (pp 1-3; in press)
- Liou, K.N. (1980), An Introduction to Atmospheric Radiation, Academic Press, San Diego.
- Liu, H.Q., and Huete, A.R., 1995, "A feedback based modification of the NDVI to minimize canopy background and atmospheric noise", IEEE Trans. Geosci. Remote Sensing, 33:457-465.
- Marchuk, G.I. (1980), The Monte Carlo Methods in Atmospheric Optics, Springer-Verlag, New York.
- Mercer, R.D., Dunkelman, L., Shaw, G. E., Larson, S. M. and Kerola, D. X. (1997), Solar spectral radiance measurements: connectivity across time and place, Proceedings of the NEWRAD'97 conference, held in Tucson, Arizona, October 27-29, 1997.
- Meyer, D., Verstraete, M. and Pinty, B., 1995. The effect of surface anisotropy and viewing geometry on the estimation of NDVI from AVHRR. Remote Sensing Reviews, 12:3-27.
- Miura T., A. Huete, van Leeuwen. W.J.D., K. Didan, 1997. Vegetation Detection Through Smoke Filled AVIRIS images: An assessment using MODIS band passes. J. Geoph. Res.. Submitted
- Moody, A. and Strahler, A.H., 1994, Characteristics of composited AVHRR data and problems in their classification. Int. J. Remote Sensing, 15(17), 3473-3491.
- Myneni, R.B. and Asrar, G., 1993, Atmospheric effects and spectral vegetation indices, Remote Sens. Environ.
- Myneni, R.B., Hall, F.G., Sellers, P.J., and Marshak, A.L., 1995, "The interpretation of spectral vegetation indices", IEEE Trans. Geosci. Remote Sens.
- Nemani, R., Pierce, L., Running, S., and Band, L., 1993. Forest ecosystem processes at the watershed scale: sensitivity to remotely-sensed Leaf Area Index estimates. Int. J. Remote Sens. 14(13): 2519-2534.
- Price, J.C., 1987. Calibration of Satellite Radiometers and the Comparison of Vegetation Indices. Rem. Sensing Environ., 21:419-422.
- Prince, S.D., 1991, A model of regional primary production for use with coarse resolution satellite data. International Journal of Remote Sensing, 12(6):1313-1330.
- Privette, J.L. Myneni, R.B., Emery, W.J. and Hall, F.G., 1996a. Optimal sampling conditions for estimating grassland parameters via reflectance model inversions. IEEE Trans. Geosci. Remote Sens. Vol. 34(1):272-284.
- Privette, J.L., Deering, D.W., and Eck, T.E., 1996b. Estimating albedo and nadir reflectance through inversion of simple BRDF models with AVHRR/MODIS-like data. J. Geoph. Res. BOREAS special issue, submitted.
- Qi, J. and Kerr, Y., 1997. On Current Compositing Algorithms. Remote Sensing Reviews, 15:235-256.

- Qi, J., Huete, A.R., Hood, J., and Kerr, Y., 1994c. Compositing Multi-temporal remote sensing data sets. PECORA 11, Symposium on land information systems, Sioux Falls August 1993. p. 206-213.
- Rahman, H., Pinty, B. and Verstraete, M.M., 1993. Coupled surface-atmosphere reflectance (CSAR) model 2. Semi-empirical surface model usable with NOAA AVHRR. *J. Geophys. Res.* 89(D11):20791-20801.
- Raich, J.W., and Schlesinger, W.H., 1992, The global carbon dioxide flux in soil respiration and its relationship to vegetation and climate, *Tellus* 44B:81-99.
- Roujean, J.L., Leroy, M., Podaire, A., and Deschamps, P.Y., 1992. Evidence of surface reflectance bidirectional effects from a NOAA/AVHRR multi-temporal data set. *Int. J. Remote Sensing* 13(4), 685-698.
- Roy, D.P., 1997. Investigation of the maximum normalized difference Vegetation Index (NDVI) and the Maximum surface temperature (T_s) AVHRR compositing procedures for the extraction of NDVI and T_s over forest. *Int. J. Remote Sens.* 18(11):2383-2401.
- Running, S.W., and Nemani, R.R, 1988, Relating seasonal patterns of the AVHRR vegetation index to simulated photosynthesis and transpiration of forest in different climates, *Remote Sens. Environ.* 24:347-367.
- Running, S.W., Justice, C., Salomonson, V., Hall, D., Barker, J., Kaufmann, Y., Strahler, A., Huete, A., Muller, J.P., VanderBilt, V., Wan, Z.M., Teillet, P. and Carneggie, D., 1994. Terrestrial Remote Sensing Science and Algorithms planned for EOS/MODIS. *Int. J. Remote Sensing*, Vol. 15, 17:3587-3620.
- Salomonson, V.V., Barnes, W.L., Maymon, P.W., Montgomery, H.E. and Ostrow, H., 1989, MODIS: advanced facility instrument for studies of the earth as a system, *IEEE Trans. Geosci. Remote Sens.* 27:145-153.
- Sellers, P.C. , 1985, Canopy Reflectance, photosynthesis and transpiration, *Int. J. Remote Sens.* 6:1335-1372
- Sellers, P.J., Tucker, C.J., Collatz, G.J., Los S., Justice, C.O., Dazlich, D.A., and Randall, D.A., 1994, "A global $1^\circ * 1^\circ$ NDVI data set for climate studies. Part 2 - The adjustment of the NDVI and generation of global fields of terrestrial biophysical parameters", *Int. J. Remote Sensing*, 15:3519-3545.
- Stowe, L.L., E.P. McClain, R. Carey, P. Pellegrino, G.G. Gutman, P. Davis, C. Long, and S. Hart. 1991. Global distribution of cloud cover derived from NOAA/AVHRR operational satellite data. *Advances in Space Research*, 3:51-54.
- Strahler, A, et al., 1996. MODIS BRDF/Albedo Product : ATBD version 4. <http://eosps0.gsfc.nasa.gov/atbd/modistables.html>.
- Tans, P.P., Fung, I.Y., and Takahashi, T. (1990), Observational constraints on the global atmosphere CO₂ budget. *Science* 247:1431-1438.
- Teillet, P.M., Staenz, K., and Williams, D.J., 1997. Effects of Spectral, Spatial , and Radiometric Characteristics on Remote Sensing Vegetation Indices of Forested Regions. *Remote Sens. Environ.* 61:139-149.

- Thome, K.J., Gellman, D.I., Parada, R.J., Biggar, S.F., Slater, P.N., and Moran, M.S. (1993), In-flight radiometric calibration of Landsat-5 Thematic Mapper from 1984 to present, in Proceedings of SPIE, vol. 1938, 126-130.
- Tomasko, M.G. and Doose, L.R. (1989), private communication.
- Townshend, J.R.G., 1994, Global data sets for land applications from the AVHRR: an introduction. *Int. J. Remote Sensing*, 15:3319-3332.
- Townshend, J.R.G., C. Justice, W. Li, C. Gurney, and J. McManus, 1991, "Global land cover classification by remote sensing: present capabilities and future possibilities", *Remote Sens. Environ.*, 35:243-256.
- Townshend, J.R.G., Justice, C.O., Gurney, C. and McManus, J., 1992, The impact of misregistration on the detection of changes in land cover, *IEEE Trans. Geosci. Remote Sens.*, 30(5):1054-1060.
- Tucker, C.J. and Sellers, P.J., 1986, Satellite remote sensing of primary productivity, *International Journal of Remote Sensing*, 7:1395-1416.
- Vermote, E., Remer, L.A., Justice, C.O., Kaufman, Y.J., and Tanré, 1995, ATBD Atmosphere correction algorithm: Spectral reflectances (MOD09), Version 2.
- Vermote, E., Tanré, D., Deuzé, J.L., Herman, M., and Mockette, J.J., 1997, Second Simulation of the Satellite Signal in the Solar Spectrum: an overview. *IEEE Trans. Geosc. Remote Sens.*, 35(3):675-686.
- Vermote, E.F., Tanre, D., Deuze, J.L., Herman, M. and Morcrette, JJ. (1997), Second simulation of the satellite signal in the solar spectrum, 6S: an overview, *IEEE Transactions on Geoscience and Remote Sensing*, 35, No. 3, 675-686.
- Vierling, L.A., Deering, D.W., Eck, T.F., 1997. Differences in Arctic Tundra Vegetation Type and Phenology as Seen Using Bidirectional Radiometry in the Early Growing Season. *Remote Sens. Environ.* 60:71-82.
- Viovy, N., Arino, O. and Belward, A.S., 1992. The best index slope extraction (BISE): A method for reducing noise in NDVI time series. *Int. J. Rem. Sensing*, Vol:13, 8:1585-1590.
- Walter-Shea, E.A., Privette, J., Cornell, D., Mesarch, M.A., Hays, C.J., 1997, Relationship between directional spectral vegetation indices and leaf area and absorbed radiation in alfalfa. *Remote Sens. Environ.* (In press)
- Walthall, C.L., Norman, J.M., Welles, J.M., Campbell, G., and Blad, B.L., 1985, Simple equation to approximate the bi-directional reflectance from vegetative canopies and bare soil surfaces," *Applied Optics*, 24(3), pp. 383-387.
- Wanner W., A.H. Strahler, B. Hu, P. Lewis, J.-P. Muller, X.. Li, C.L. Barker Schaaf, and M.J. Barnsley, 1997. Global retrieval of bidirectional reflectance and albedo over land from EOS MODIS and MISR data: Theory and algorithm. *J. Geoph. Res.*, 102, D14, 17143-17161.
- Wanner W., X.. Li, A.H. Strahler, 1995. On the Derivation of kernel-driven models of bidirectional reflectance. *J. Geoph. Res.*, 100, D10, 21077-21089
- Wolfe. R., D. Roy. Georegistration of MODIS data (level 2G), to be submitted

Wu, A., Li, Z. and Cihlar, 1995, Effects of land cover type and greenness on advanced very high resolution radiometer bidirectional reflectances: Analysis and removal. *J. Geophys. Res.*, 100(D5), 9179-9192.

E. APPENDIX 1

Summary of the ESFT Technique: Application to CH₄ Absorption in Saturn for the $\lambda = 1.7 - 2.6 \mu\text{m}$ Spectral Region

The “exponential-sum-fitting of transmittances” (ESFT) technique has been in general use for some time as a numerical means for evaluating absorption coefficients for a variety of molecular species. The ESFT method is especially attractive for use in the determination of effective absorption coefficients for gases in planetary atmospheres where the multiple scattering of light by haze and cloud aerosols is important. A host of “band-model” formulations for calculating the transmittance of sunlight through layers of “clean” gas abound. Such parameterization of line strength and line spacing for complex absorption bands like those exhibited by CH₄ and H₂O is quite satisfactory for traditional RLM studies of planetary atmospheres. But as soon as small particles are envisaged to be mixed-in with the gaseous constituents, band-model representations of spectral line optical depths are rendered intractable for use in scattering models.

The underlying rationale for adopting the ESFT approach is as follows: because there is no correlation whatsoever between the magnitude of the absorption coefficient and the frequency of the radiation, a transformation can be made from $k(\nu)$ to $k(u)$, i.e., the absorption coefficient as a function of frequency can be recast as an “effective” absorption coefficient, k_{eff} , which is a function of the optical path u . The transmittance is:

$$T(u) = (\Delta\nu)^{-1} \int \exp(-k_{\nu}u) d\nu$$

The ESFT methodology is not too dissimilar from an approach known as the “ k -distribution”. As Goody and Yung (1989) point out, it is sufficient to know what fraction $f(k)dk$ of the frequency domain ν can be represented by absorption coefficients between k and $k + dk$. No importance is attached to the location in frequency space of a given value of k . An expression entirely is:

$$T(u) = \int f(k) \exp(-ku) dk$$

where $f(k)dk$ is the k -distribution function. It is readily recognizable that $f(k)$ is the inverse Laplace transform of $T(u)$.

The ESFT approach circumvents the necessity of evaluating the in-verse Laplace transform. ESFT is inherently a numerical analysis problem, and as such it is intrinsically ill-conditioned. The specific set of algorithms we used to determine the effective CH₄ k's, originated with Asano and Uchiyama (1987). They have extended the traditional ESFT technique to incorporate an iterative non-linear least squares fitting of an ordered set of the effective k's. The work of Asano and Uchiyama represents an improvement in a real, practical sense over many previous implementations of the ESFT technique. Their approach relies on the pre-selection of a set of weights, w_i , such that

$$T(u) \cong \sum w_i \exp(-k_i u)$$

These weights can be quite accurately determined once a preferred quadrature scheme is adopted. The heart of the Asano and Uchiyama ESFT procedure is the successive correction of the k_i 's for the set of fixed w_i 's. The virtue of this extended ESFT technique is its ability to find a best-fitting set of k_i 's for a wide range of absorber amounts, u , which might not necessarily be equally spaced.

Kerola (1989, private contributions) developed the FORTRAN code. It was implemented in conjunction with Tomasko for modeling CH₄ absorptions in Titan's near-IR and visible spectrum. The program was structured in a fashion to permit direct assessment of the standard deviation of the transmittances computed via ESFT versus those obtained from wide-band laboratory measurements of transmittances made at NASA Ames Research Center. The Ames laboratory data was generated by Giver (1990). Best-fit values for a monochromatic absorption coefficient, k_v , and a pressure coefficient, y_v , were obtained by Giver from comparison of his experimental data to that given in the Malkmus random-band model. The transmittance in the Malkmus model is:

$$T_M = \exp\left(-2\pi y_v p \left(\left[\frac{k_v u}{\pi y_v p} + 1 \right]^{1/2} - 1 \right)\right)$$

The pressure parameter, y_v , is the ratio of the line width at 1 atmosphere to the mean line spacing. It has units of atm⁻¹. The atmospheric pressure is p (in atm). The Ames measurements were made at 3 temperatures: $T = 112$ K, 188 K, and 295 K. The full Ames dataset extends from about 3770 cm⁻¹ to close to 9000 cm⁻¹. The spectral transmittances are recorded at every 10 cm⁻¹. In

our Saturn modeling (Kerola, 1994), we performed the exponential-sum fitting on spectral intervals 50 cm^{-1} wide, spanning the region $3785 - 5995 \text{ cm}^{-1}$. Our efforts included only the low and mid-temperature Ames datasets. We used a linear extrapolation of the k_i 's over temperature. For most of the CH_4 bands, the effective levels probed in Saturn's troposphere are slightly colder than about 100 K.

As a matter of computational ease and accuracy, the ESFT code was designed to use 8-point Gaussian quadrature for the determination of the weights. The most important final output of the program is a set of 8 best-fit ESFT k 's. These "equivalent" absorption coefficients are arranged so that they are in ascending order (i.e, $k_1 < k_2 < k_3$, etc). 8 k_i values are generated for each spectral interval ($\Delta\nu = 50 \text{ cm}^{-1}$), and for each atmospheric pressure p . For each spectral interval, $T_M(u_i)$ is computed using equal spacing in the logarithm of absorber amount. The initial guess for the absorption coefficient is given by:

$$k_i^{(0)} = \frac{\ln T_i}{u_i}$$

60 values of u_i were calculated. Two conditions of convergence involve either iterating at most 100 times or ending the iterations when the relative RMS. error is less than 0.2 percent. Convergence is often quite rapid, taking typically less than a couple dozen iterations for most spectral bands, and for most pressures.